Is the outflow-layer inertial stability crucial to the energy cycle and development of tropical cyclones?

Yuanlong Li[1], Yuqing Wang[2*], Zhe-Min Tan[1]

[1]Key Laboratory for Mesoscale Severe Weather/MOE, and School of Atmospheric Sciences, Nanjing University, Nanjing, China
[2]International Pacific Research Center and Department of Atmospheric Sciences, School of Ocean and Earth Science and Technology, University of Hawaii at Mānoa, Honolulu, Hawaii, USA

25 August, 2022 (submitted)

6 January 2023 (first revised)

15 March 2023 (second revised)

Dateline

Submitted to ***Journal of the Atmospheric Sciences***

*Corresponding author address:
Prof. Yuqing Wang
International Pacific Research Center
University of Hawaii at Manoa
404A/POST, 1680 East West Road,
Honolulu, HI 96822, USA.
Email: yuqing@hawaii.edu

ABSTRACT

This study revisits the issue of why tropical cyclones (TCs) develop more rapidly at lower latitudes, using ensemble axisymmetric numerical simulations and energy diagnostics based on the isentropic analysis, with the focus on the relative importance of the outflow-layer and boundary-layer inertial stabilities to TC intensification and energy cycle. Results show that although lowering the outflow-layer Coriolis parameter and thus inertial stability can slightly strengthen the outflow, it does not affect the simulated TC development, whereas lowering the boundary-layer Coriolis parameter largely enhances the secondary circulation and TC intensification as in the experiment with a reduced Coriolis parameter throughout the model atmosphere. This suggests that TC outflow is more likely a passive result of the convergent inflow in the boundary layer and convective updraft in the eyewall.

The boundary-layer inertial stability is found to control the convergent inflow in the boundary layer and depth of convection in the eyewall and thus the temperature of energy sink in the TC heat engine, which determines the efficiency and overall mechanical output of heat engine and thus TC intensification. It is also shown that the hypothesized isothermal and adiabatic compression legs at the downstream end of the outflow in the classical Carnot cycle is not supported in the thermodynamic cycle of the simulated TCs, implying that the assumed TC Carnot cycle is not closed. It is the theoretical maximum work of heat engine, not the energy expenditure following the outflow downstream, that determines the mechanical work used to intensify a TC.

1. Introduction

The outflow layer in the upper troposphere generally between 100 and 300 hPa is the outward branch of the secondary circulation of a tropical cyclone (TC) and is related to TC intensity changes (McBride 1981; Wang 2007; Oyama 2017). There are several explanations in the literature as to how the outflow-layer dynamics affect TC development. For example, the outflow may remove the inner-core mass or warm air and thus maintain the inner-core convective instability (Holland and Merrill 1984; Shi et al. 1990; Chen and Gray 1985; Wu and Cheng 1999) or push back against the environmental winds and thus reduce the local vertical wind shear (Xu and Wang 2013; Ryglicki et al. 2019; Dai et al. 2021; Shi and Chen 2021). In addition, the eddy momentum flux in the outflow layer may enhance TC's secondary circulation by a deep balanced response and thus favors the eyewall convection and TC intensification (Challa and Pfeffer 1980; Holland and Merrill 1984; Wu and Cheng 1999; Chen et al. 2015; Ditchek et al. 2017).

The upper-tropospheric outflow is also part of the TC Carnot cycle (Emanuel 1986; Pauluis and Zhang 2017). Emanuel (1986, 1991) succinctly divided the TC Carnot cycle into four legs. In leg 1 the near-surface ambient air parcel spirals toward the TC eyewall with isothermal expansion and gains enthalpy from the sea surface. In leg 2 the air parcel ascends in the TC's eyewall and then flows out to large radius with moist-neutral adiabatic expansion. The term "moist-neutral adiabatic" means a state in which the absolute angular momentum and saturation entropy surfaces are congruent. In leg 3 the air parcel descends following the outflow downstream with isothermal compression and loses entropy by infrared radiation. In leg 4 the air parcel further descends to the starting point of leg 1 with moist-neutral adiabatic compression to close the cycle. For simplicity, Emanuel (1986, 1991) omitted the hydrologic cycle in the hypothesized TC (Pauluis 2011) and assumed the work produced by the Carnot cycle is mainly consumed to offset the mechanical dissipation in the boundary layer (leg 1) by surface friction as well as at large radii in the outflow layer (leg 3) by restoring the outflow's absolute angular momentum to its ambient value. This framework means that the outflow layer may affect the TC Carnot cycle or TC development by mechanical dissipation. The outflow-layer mechanical dissipation was omitted in the latest formulation of the Carnot cycle in Emanuel (1997, 2018) and Rousseau-Rizzi and Emanuel (2019) in deriving a closed expression of TC potential intensity.

One important factor influencing the TC outflow is the local inertial stability. A lower inertial stability implies a weaker resistance to axisymmetric radial motion, with which the outflow air may exhaust/ventilate at a larger radius (Rappin et al. 2011; O'Neill and Chavas 2020). Rappin et al. (2011) further argued that as the outflow air exhausts at a larger radius, the work to "force" subsidence in leg 3 of the Carnot cycle in Emanuel (1986, 1991) would be reduced more by additional radiative cooling. Although the infrared radiative cooling-associated subsidence is often comparable with the actual subsidence in the outer core of a TC (Emanuel 2004; Wang and Lin 2020), the work of subsidence has never been characterized in the Carnot cycle, and the "forced subsidence" could not be found in previous studies as pointed out by O'Neill and Chavas (2020). However, the simulations in Rappin et al. (2011) did show that with a lower latitude or weaker environmental inertial stability, the TC outflow is more intense and the TC intensifies more rapidly, with a lesser difference in absolute angular momentum between the defined outflow air and the environmental air. They thus hypothesized that inertial stability may affect TC development by modulating the outflow-layer mechanical dissipation. Emanuel (1986) also assumed that by reducing the outflow-layer mechanical dissipation, more energy is available to overcome surface friction in the boundary layer. Nevertheless, the role of outflow-layer mechanical dissipation on the overall energy conversion and the role of inertial stability on outflow-layer mechanical dissipation have not been quantified in the literature. Note that in addition to the outflow, the lower inertial stability can also facilitate the boundary-layer inflow, leading to a stronger overall secondary circulation (e.g., Kepert and Wang 2001; Li and Wang 2021b). Therefore, although the phenomenon that a TC intensifies more rapidly with a lower latitude (or environmental inertial stability) has been widely confirmed (e.g., DeMaria and Pickle 1988; Rappin et al. 2011; Li et al. 2011; Smith et al. 2015), it is unclear whether this dependence is dominated by inertial stability in the outflow layer or the boundary layer.

The key to understanding the TC energy cycle and development based on the concept of Carnot cycle is how a closed thermodynamic cycle is defined/assumed, as air parcel's movement in the TC secondary circulation is often highly turbulent and not a closed cycle. In addition, for the Carnot cycle proposed by Emanuel (1986, 1991), the isothermal compression in leg 3 is hard to be found in natural TCs, because of the marked thermal stratification in the outflow layer associated with the local small-scale turbulence (Emanuel and Rotunno 2011; Emanuel 2012; Molinari et al. 2015; Komaromi and Doyle 2017). In addition, the assumption of moist-neutral adiabatic descent in the outer region (leg 4) is not confirmed in previous studies, and the state of moist neutrality is often only confined in the inner core of TCs during their mature phase (Peng et al. 2018; Wang et al. 2021; Wang and Lin 2021). Recently, a novel methodology based on the isentropic analysis, named Mean Airflow as Lagrangian Dynamics Approximation (MAFALDA), was introduced to circumvent the aforementioned issues (Pauluis and Mrowiec 2013; Pauluis 2016; Mrowiec et al. 2016). The main assumption of MAFALDA is that the thermodynamic cycles of actual parcel trajectories can be approximated by the isolines of the streamfunction in isentropic coordinates (equivalent potential temperature versus height, $\theta_e - z$), based on the conservation property of θ_e. With MAFALDA, the thermodynamic cycle of an air parcel in the temperature versus specific entropy diagram is consecutive, and thus the extreme isothermal or moist-neutral adiabatic assumptions in the Carnot cycle hypothesized in Emanuel (1986, 1991) can be relaxed. Previous studies have shown that MAFALDA can capture well the key aspects of parcel trajectories and the MADALDA-based energy diagnostics can also depict well the essential characteristics of energy conversion during TC development (e.g., Pauluis 2016; Pauluis and Zhang 2017; Fang et al. 2019).

In this study, the role of environmental inertial stability on the energy cycle and TC development is revisited based on a suite of ensemble axisymmetric TC simulations and energy diagnostics using MAFALDA. The main objectives are threefold: to examine whether the outflow-layer inertial stability is crucial to outflow strength or TC development, to evaluate the role of outflow-layer mechanical dissipation on TC energy cycle, and to provide a more complete understanding of how environmental inertial stability affects TC development based on the viewpoint of energetics. The remainder of the paper is organized as follows. Section 2 describes the model setup and experimental design. Section 3 gives an overview of results from the ensemble experiments. The MAFALDA-based energy diagnostics are detailed in section 4. Main conclusions are summarized and discussed in section 5.

2. Model setup and experimental design

The main results in this study are based on idealized simulations using the axisymmetric cloud model, CM1, version 20.3 (Bryan and Fritsch 2002). The model settings are identical to those used in Li et al. (2020). The model domain is 3100 km in the radial direction with a grid spacing of 1 km within 100-km radius and linearly stretched to 14 km at the lateral boundary. There are 59 vertical levels with stretched grids below 5.5 km and 0.5 km from 5.5 to 25 km. The sea surface temperature is 29°C and the corresponding atmospheric sounding is that sorted over the western North Pacific as in Li et al. (2020). The cloud microphysics scheme is the Thompson et al. (2008) double-moment scheme. Newtonian cooling, capped at 2 K day^{-1}, is used to mimic radiative cooling as in Rotunno and Emanuel (1987) and Wang (2007). The Smagorinsky-type diffusion scheme (Bryan and Fritsch 2002) is used to parameterize subgrid-scale turbulent mixing, with the horizontal and asymptotic vertical mixing lengths fixed at 700 m (Zhang and Montgomery 2012) and 70 m (Zhang and Drennan 2012), respectively. The surface enthalpy exchange coefficient is set to 1.2×10^{-3} (Black et al. 2007), while the surface drag coefficient initially increases with the 10-m wind speed up to 25 m s^{-1} and is then kept constant at 2.4×10^{-3} afterwards (Donelan et al. 2004).

The inertial stability projected onto an axisymmetric vortex can be written as

$$I^2 = \frac{1}{r^3}\frac{\partial M^2}{\partial r} = (f + \frac{2v}{r})(f + \frac{\partial rv}{r\partial r}), \tag{1}$$

where r is radius, v tangential wind speed, f the Coriolis parameter at a given latitude, and M the absolute angular momentum [$M = rv + (1/2)fr^2$]. Based on Eq. (1), the background inertial stability in the TC environment can be modulated by changing either the Coriolis parameter (namely latitude) or environmental circulation, such as the zonal westerly jet or trough from the mid-latitude poleward of a TC (Black and Anthes 1971; Rappin et al. 2011), or both. Here, we focus on the internal dynamics of TCs and do not consider the multiscale interactions between a TC and its environment. Therefore, as in Rappin et al. (2011) and O'Neill and Chavas (2020), we vary environmental inertial stability by varying f in a quiescent environment. Similar to Rappin et al. (2011), two values of f correspond to the latitudes of 10ºN and 30ºN are used throughout the model atmosphere, labeled as All_10N and All_30N, respectively. To investigate whether the differences between experiments All_10N and All_30N are dominated by the difference in inertial stability in the outflow layer or in the boundary layer, two sensitivity experiments are performed as All_30N but with f above 10 km and below 2 km height being reduced to that at 10ºN, respectively, labeled as OL_10N and BL_10N. We choose the two heights because the outflow layer and inflow layer in our simulated TCs are mainly above 10 km and below 2 km, respectively. They are also roughly consistent with observations in intensifying and mature TCs. Our preliminary tests indicate that the main conclusions from this study are insensitive to the two heights in reasonable ranges. An additional experiment as All_30N but with f in the layer between 2–10 km heights reduced to that at 10ºN, labeled as ML_10N, is also performed to assess the effect of middle-layer inertial stability on TC development.

For each experiment, 21 ensemble runs are performed as described in Li et al. (2020). In the standard run, the initial maximum tangential wind speed is 15 m s^{-1} at the surface with the radius of maximum wind (RMW) of 80 km, and the radial profile of tangential wind speed is calculated based on the algorithm in Wood and White (2011) with the radial shape parameter of 1.6. The remaining 20 runs are generated by consecutively perturbing the initial maximum tangential wind speed by an increment of ± 0.1 m s^{-1} (for 10 runs) or the initial RMW by ± 0.4 km (for 10 runs). Note that for a given initial tangential wind distribution, the mass field at each model level is in gradient wind balance with the corresponding Coriolis parameter at the initial time. All runs are integrated for 240 h with hourly output. The results discussed below are mainly based on the ensemble mean to minimize the effect of model internal variability on our main conclusions.

3. An overview of the simulation results

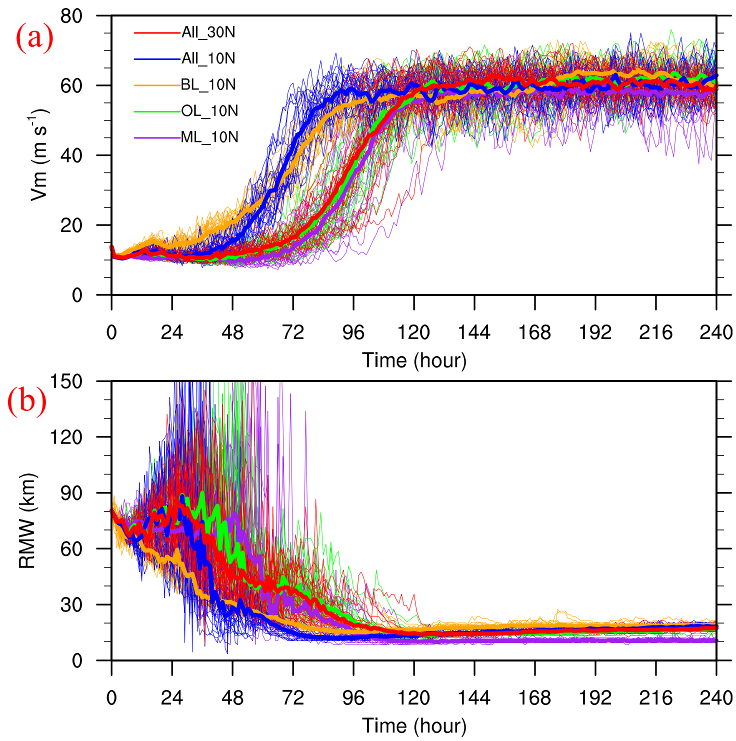

Figure 1. Time series of (a) the maximum 10-m total wind speed and (b) the corresponding RMW with results from the 21 individual simulations and the ensemble mean shown in thin and thick curves, respectively, for the five experiments, All_30N, All_10N, BL_10N, OL_10N, and ML_10N.

Figure 1 displays the time series of the maximum 10-m total wind speeds and the RMWs of all individual ensemble simulations and ensemble mean for the five axisymmetric experiments described in section 2. Consistent with previous studies (e.g., DeMaria and Pickle 1988; Rappin et al. 2011; Li et al. 2011; Smith et al. 2015), the TC with lower global environmental inertial stability (All_10N) develops more rapidly and reaches the quasi-steady state earlier than that with higher global environmental inertial stability (All_30N). The TCs in All_10N and All_30N experiments start to intensify rapidly around 36 h and 66 h, and reaches the quasi-steady state around 90 h and 120 h of simulations, respectively (Fig. 1a). The RMW also contracts earlier in All_10N than in All_30N, and for all experiments, the rapid contraction precedes the rapid intensification (Fig. 1b) as found in idealized numerical simulations and in observations analyzed in Li at al. (2021, 2022).

A new finding is that lowering the outflow-layer inertial stability has little effect on the TC development (compare All_30N and OL_10N), whereas lowering the boundary-layer inertial stability leads to a much earlier intensification and earlier RMW contraction (compare All_30N and BL_10N), and the TC in BL_10N reaches a quasi-steady state around 90 h of the simulation, similar to those in All_10N (Fig. 1). This means that although the lower inertial stability throughout the atmosphere in All_10N may facilitate both the boundary-layer inflow (DeMaria and Pickle 1988; Rappin et al. 2011; Smith et al. 2015) and upper-layer outflow (Rappin et al. 2011), it is the lower boundary-layer inertial stability that predominantly leads to the earlier TC development in All_10N than in All_30N.

It is also found that the TC in BL_10N starts to intensify earlier than that in All_10N. The earlier intensification in BL_10N can be explained by the higher inertial stability in the middle-layer and thus stronger feedback between TC circulation and diabatic heating in BL_10N than in All_10N as inferred from the balanced vortex dynamics as demonstrated by Schubert and Hack (1982) and Vigh and Schubert (2009). As shown in Fig.1a, lowering the middle-layer Coriolis parameter in ML_10N delays the onset of TC intensification but its effect on the subsequent intensification of the TC is very marginal. This is mainly because the Coriolis parameter affects the inertial stability more significantly when the TC vortex is at its weak stage during which vertical relative vorticity is relatively small. However, after the onset of intensification, the inertial stability will be largely determined by the relative vorticity and the intensification rate of the simulated TC would be largely determined by the strength and radial location of eyewall heating, which is largely controlled by the boundary layer dynamics (e.g., Li and Wang 2021a,b). Therefore, the results from the additional experiment ML_10N further confirm that the faster development in All_10N than in All_30N is primarily due to the lower boundary-layer inertial stability. In the following discussion, we will focus on the four experiments, i.e., All_30N, All_10N, BL_10N, and OL_10N, to further investigate the relative importance of the outflow-layer and boundary-layer inertial stabilities to the TC development and energy cycle.

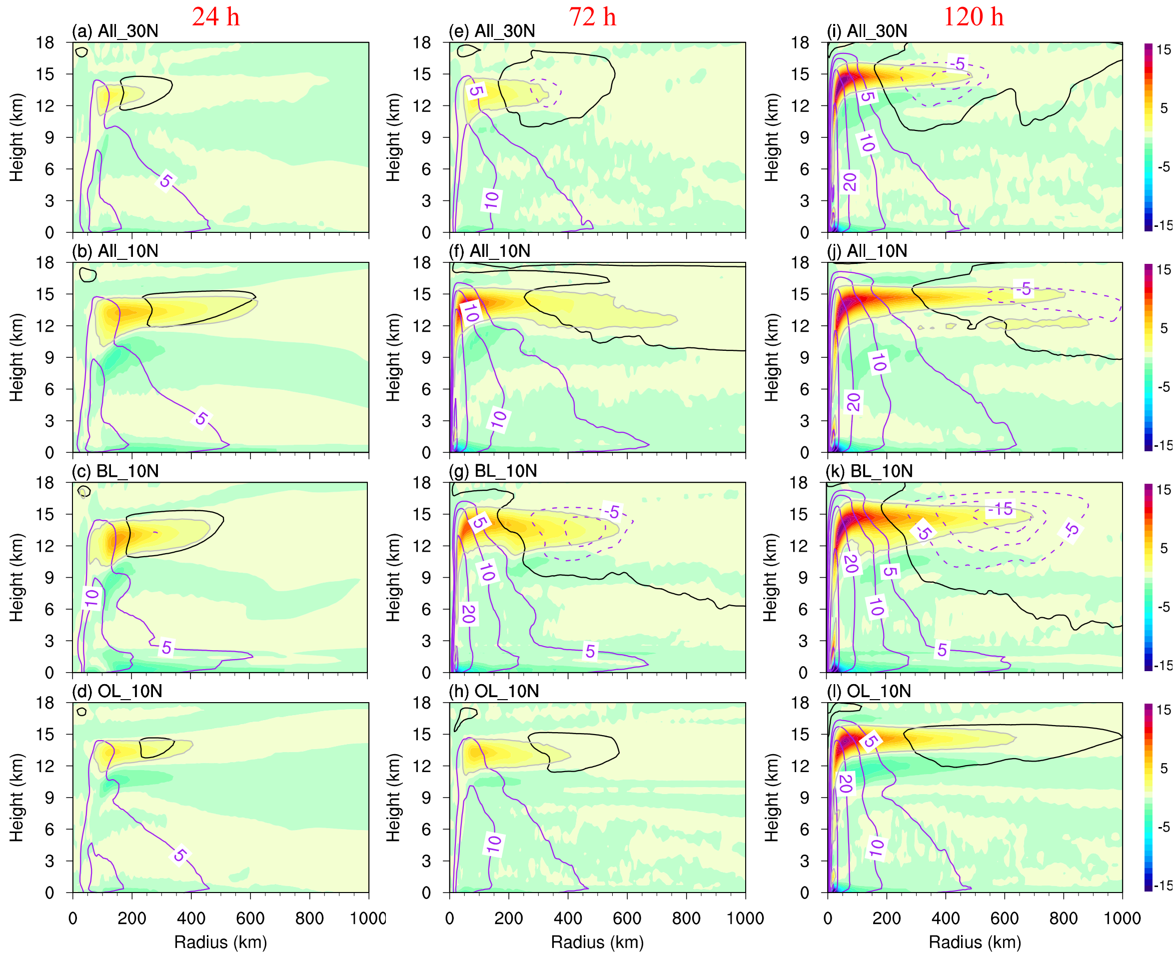

Figure 2. Radial-vertical cross sections of the ensemble-mean tangential winds (purple contours with zero contour highlighted in black and negative values dashed; m s^{-1}), and radial winds (shading with 1 m s^{-1} contour highlighted in grey) at 24, 72, and 120 h of simulations in experiments from the top down All_30N, All_10N, BL_10N, and OL_10N.

To understand how inertial stability affects TC development, we first compare in Fig. 2 the evolution of the ensemble-mean wind structures in the four experiments. Consistent with the results in Rappin et al. (2011) and O'Neill and Chavas (2020), the outflow is more intense and expands to a larger radius in All_10N than in All_30N during all development stages (Figs. 2a–b, e–f, i–j), even during the initial spinup period when the TCs in the two experiments have similar intensities (Fig. 1a; Figs. 2a–b). Rappin et al. (2011) ascribed the more intense outflow in the lower-latitude experiment to the weaker inertial stability in the outflow layer and thus weaker resistance to the outward expansion of the upper-level outflow in the simulated TC. O'Neill and Chavas (2020) also showed that the outer radius of outflow in an idealized radiative-convective equilibrium state can be scaled with the Rossby deformation radius, which is inversely proportional to the local inertial stability. However, our results show that the more intense outflow still occurs in BL_10N even with the outflow-layer inertial stability unchanged (Figs. 2c,g,k); while lowering the outflow-layer inertial stability in OL_10N only slightly enhances the outflow (Figs. 2d,h,l) compared with that in All_30N (Figs. 2a,e,i), but much less obvious than lowering the inertial stability in the boundary layer in BL_10N (Figs. 2c,g,k). These results indicate that the stronger secondary circulation and thus outflow in the lower latitude simulation or lower environmental inertial stability is mainly due to the lower inertial stability in the boundary layer rather than in the outflow layer. The weak resistance to convergent inflow allows for a more intense inflow in the boundary layer (DeMaria and Pickle 1988; Li et al; 2012; Figs. 2a–c, 2e–g, 2i–k), which could facilitate more vigorous vertical motion and convection in the eyewall, forcing a stronger outflow. As a result, the overall secondary circulation is stronger and the TC intensifies earlier in the experiment with lowering inertial stability in the boundary layer (Fig. 1).

To confirm the sequence of events described above, the multilevel TC boundary layer model simplified from that in Kepert and Wang (2001) and used in Li and Wang (2021a,b) and Fei et al. (2021) is used to conduct several experiments. Similar to that in our CM1 simulations, the horizontal and asymptotic vertical mixing lengths are fixed at 700 m and 70 m, respectively, and the wind-dependent surface drag coefficient of Donelan et al. (2004) is used in the boundary layer model. The model is 2500 km in radius with a constant grid spacing of 1 km. There are 23 vertical levels with stretched grids from 10 m to 2.2-km height. Figure 3 shows the steady-state response of the radial wind and vertical motion to a specified TC-like vortex with a maximum tangential wind speed of 20 m s^{-1} at a radius of 40 km at the model top in two experiments with the Coriolis parameter at 10ºN and 30ºN, respectively. We can see that with the lower latitude, both the boundary-layer inflow and vertical motion inside the RMW become stronger, similar to the result from the slab boundary layer model in Smith et al. (2015). This further confirms that the sensitivity of the simulated secondary circulation and the onset of intensification to the latitude in CM1 shown in Figs. 1 and 2 is a result of the change of latitude in the boundary layer.

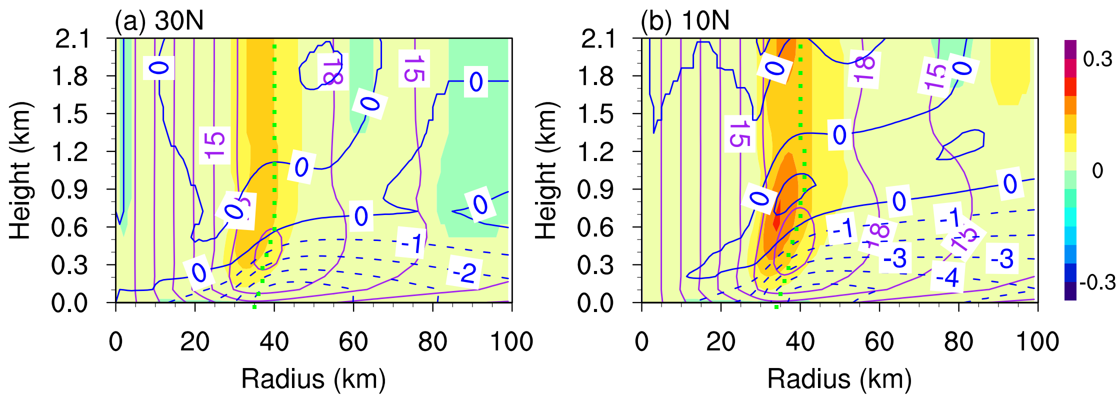

Figure 3. Radial-vertical cross sections of the steady-state boundary layer radial wind (blue contours with negative value dashed; m s^{-1}) and vertical velocity (shading; m s^{-1}) in response to a specified TC-like vortex at the model top in the multilevel boundary layer model from runs at a latitude of (a) 30°N and (b) 10°N.

In addition, we can see from Fig. 2 that the anticyclone downstream of the outflow is stronger (weaker) in BL_10N (OL_10N) than in All_30N. This can be explained by the conservation of absolute angular momentum [i.e., $M = rv + (1/2)fr^2$]. Namely, as the air parcel moves radially outward in the outflow layer, the cyclonic tangential wind will decrease and turn to anticyclonic at large radii. Under a smaller outflow-layer f, the decrease of tangential wind with radius will be slower, resulting in a weaker anticyclone in OL_10N than in All_30N. With a similar outflow-layer f, the smaller boundary-layer f indicates a weaker source of M from the boundary layer, and stronger eyewall updraft and outflow as mentioned earlier (Figs. 2 and 3). Considering the conservation of M as air parcel moves out of the boundary layer into the eyewall and outflow downstream, both the weaker source of M and stronger outflow could result in the stronger anticyclone in BL_10N than in All_30N. This further suggests that the outflow is critically related to the boundary-layer inflow. Therefore, our results suggest that the TC outflow is more likely a passive result of the boundary-layer convergent inflow and eyewall updraft rather than a direct response to the local inertial stability in the outflow layer as argued in previous studies (Black and Anthes 1971; Rappin et al. 2011; Komaromi and Doyle 2018; O'Neill and Chavas 2020).

4. Energetics diagnostics

Results from section 3 indicate that the outflow-layer inertial stability has little effect on TC development, which is in contrast with the hypothesis by Rappin et al. (2011). In this section, we further investigate the roles of inertial stability and mechanical dissipation following the outflow downstream on the simulated TC energetics, as proposed by Rappin et al. (2011) (see Introduction).

a. A revisit of TC Carnot's theorem

As described in Emanuel (1986, 1991), the TC Carnot heat engine can be formulated from Bernoulli's equation and the first law of thermodynamics. Along air parcel's trajectories the former can be written as

$$d\left(\frac{1}{2}|\boldsymbol{V}|^2\right) + d(\Gamma z) + \alpha_d dp + \boldsymbol{F}\cdot d\boldsymbol{l} + \Gamma r_T dz = 0, \tag{2}$$

where $|\boldsymbol{V}|$ is the total wind speed, Γ the acceleration of gravity, α_d the specific volume of dry air, p the pressure, $\boldsymbol{F}$ the viscous drag force per unit mass of dry air, $\boldsymbol{l}$ the air parcel's trajectories and r_T the mixing ratio of total water. Note that Eq. (2) is similar to Eq. (1) in Emanuel (1991), but with the frictional dissipation by falling hydrometeors included, which can be estimated by the work done to lift water substance (Pauluis et al. 2000; Pauluis and Held 2002a,b), i.e., the last term on the lhs of Eq. (2). The first law of thermodynamics in a moist system can be written as

$$Tds = dh - \alpha_d dp - \sum_{w=v,l,i} g_w dr_w, \tag{3}$$

where T is the air temperature, s and h the moist entropy and enthalpy per unit mass of dry air, g_v, g_l, and g_i the specific Gibbs free energy for water vapor, liquid water, and ice, and r_v, r_l, and r_i the mixing ratio of water vapor, liquid water, and ice, respectively. The detailed definition of entropy and Gibbs free energy are given in the appendix (or see Pauluis 2011; 2016; Pauluis and Zhang 2017). The inclusion of Gibbs penalty in Eq. (3) is to take into account of the work that the heat engine fails to produce due to the thermodynamic irreversible processes associated with the hydrological cycle such as diffusion of water vapor and phase changes (Pauluis and Held 2002a,b; Pauluis 2011).

Eliminating $\alpha_d dp$ in Eq. (2) using Eq. (3) and integrating the resultant equation over a closed thermodynamic cycle gives

$$\underbrace{\oint T ds}_{W_{max}} = \underbrace{\oint \boldsymbol{F} \cdot d\boldsymbol{l}}_{W_{KE}} + \underbrace{\oint \Gamma r_T dz}_{W_P} \underbrace{- \oint \sum_{w=v,l,i} g_w dr_w}_{G_P} , \tag{4}$$

where W_{KE} can be obtained by integrating Eq. (2) as

$$W_{KE} = -\oint \alpha_d dp - W_P. \tag{5}$$

In (4) and (5), each term describes a work per unit mass of dry air circulating the thermodynamic cycle. W_{max} denotes the theoretical maximum work a Carnot heat engine can produce, equivalent to the net external heating from surface enthalpy flux, radiative heating or cooling, dissipative heating, and turbulent mixings. W_{KE} is the total dry air-associated mechanical dissipation in the cycle, i.e., the representation of the total kinetic energy produced by the heat engine. W_P denotes the total work done to lift water substance in the cycle. W_{KE} and W_P are the total mechanical output in the cycle. G_P is the total Gibbs penalty in the cycle. Since water added to the cycle is often unsaturated at low Gibbs free energy but the water removed from the cycle is often saturated at high Gibbs free energy (Pauluis 2011; 2016; Pauluis and Zhang 2017), G_P is positive definite (see appendix Eqs. A3a–c). Therefore, both W_P and G_P from the hydrological cycle limit the generation of kinetic energy in the Carnot cycle.

Emanuel (1986, 1991) qualitatively divided the TC Carnot cycle in Eulerian coordinates into four legs as mentioned in section 1 and assumed mechanical dissipation mainly occurs in both the boundary layer (leg 1) and the outflow layer (leg 3). Based on Eq. (2), considering the hydrostatic relation and omitting the frictional dissipation by falling hydrometeors, Emanuel (1986, 1991) formulated the outflow-layer mechanical dissipation in descending leg 3 as

$$\int_o^{o'} \boldsymbol{F} \cdot d\boldsymbol{l} \approx -\int_o^{o'} d\left(\frac{1}{2}|\boldsymbol{V}|^2\right) = -\Delta \frac{1}{2}\left(\frac{M}{r} - \frac{1}{2} f r\right)^2 \Big|_o^{o'}, \tag{6}$$

where o and o' denote the start and end points of leg 3. Rappin et al. (2011) estimated the outflow-layer mechanical dissipation in the experiments with different latitudes using Eq. (6), with the ambient absolute angular momentum $M_{o'}$ assumed to be equal to the 500-km M near the surface. They showed that the so-defined outflow-layer mechanical dissipation is lower in the lower latitude experiment, corresponding to a more rapid TC intensification. They thus argued that in a lower latitude, the outflow air ventilates at a larger radius due to the weaker outflow-layer inertial stability, which reduces the outflow-layer mechanical dissipation, and thus more energy is available to overcome frictional dissipation in the boundary layer as in Eq. (4) with W_P and G_P omitted. Although the results in section 3 have clarified that the outflow intensity mainly depends on the boundary-layer rather than the outflow-layer inertial stability, it is still unclear whether the outflow-layer mechanical dissipation can affect the TC development.

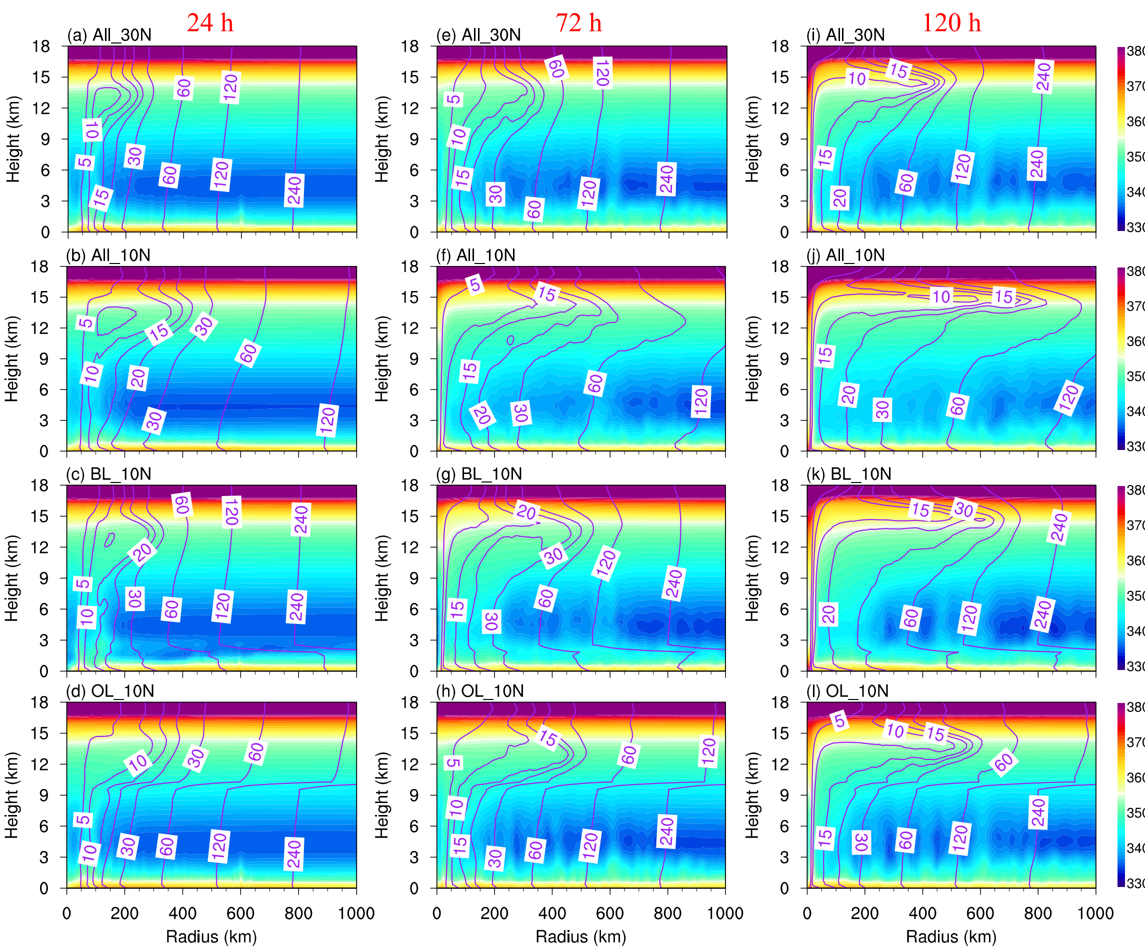

Figure 4. Radial-vertical cross sections of the ensemble-mean equivalent potential temperature calculated using Eq. (A4) (shading; K) and absolute angular momentum (purple contours; 10^5 m^2 s^{-1}) in the four experiments.

One important implicit assumption discussed in Rappin et al. (2011) is that the TC Carnot cycle exactly follows the four legs proposed by Emanual (1986, 1991), i.e., isothermal expansion and compression in leg 1 and leg 3, and moist-neutral adiabatic expansion and compression in leg

2 and leg 4. However, there is a marked thermal stratification in temperature (not shown), as that in θ_e (Fig. 4), in the outflow layer in all experiments, indicating that the isothermal compression following the outflow downstream (leg 3) is hard to occur. The moist-neutral adiabatic compression, i.e., leg 4, is also hard to be characterized, as the M and θ_e surfaces are not congruent and are even nearly orthogonal over the outer-core regions in the troposphere (Fig. 4). Therefore, it is hard to estimate the outflow-layer mechanical dissipation from Eq. (6). In addition, without a closed Carnot cycle, the theoretical maximum work W_{max} that constrains the total mechanical dissipation W_{KE} is hard to be estimated, and it is thus hard to evaluate whether the boundary-layer mechanical dissipation depends on the outflow-layer mechanical dissipation based on the classical Carnot's theorem.

b. MAFALDA Trajectories

Following previous studies (Pauluis and Mrowiec 2013; Pauluis 2016; Mrowiec et al. 2016; Pauluis and Zhang 2017), MAFALDA is applied to extract thermodynamic cycles in the simulated TCs. By MAFALDA, parcel trajectories are defined as the isolines of isentropic streamfunction in isentropic coordinates. Similar to that in Pauluis (2016), the equivalent potential temperature θ_e is defined with respect to ice (Eq. A4; Fig. 4). For any variable $a(r, z, t)$ in Eulerian coordinates, we can transform it into isentropic coordinates as $\langle a \rangle_{\theta_e}$ by

$$\langle a \rangle_{\theta_e}(\theta_e, z, t) = \int_0^L \langle a \rangle(\theta_e, z, r, t)\, dr, \qquad (7)$$

with

$$\langle a \rangle(\theta_{e0}, z, r_0, t) = 2\pi r_0 \int_0^L a(r, z, t)\, \sigma\{\theta_{e0} - \theta_e(r, z, t)\}\sigma\{r - r_0\} dr,$$

where $\sigma\{\cdot\}$ is the Dirac delta function, and $L = 1000$ km is the radius used to the integral in Eulerian coordinates. The results below are qualitatively unchanged for $L = 1500$ or 2000 km. Then the isentropic streamfunction Ψ_{θ_e} in isentropic coordinates is computed as the integral of the vertical mass flux $\langle \rho w' \rangle_{\theta_e}$ (Pauluis and Mrowiec 2013; Pauluis 2016)

$$\Psi_{\theta_e}(\theta_e, z, t) = \int_0^{\theta_e} \langle \rho w' \rangle_{\theta_e}(\theta_e', z, t) d\theta_e', \qquad (8)$$

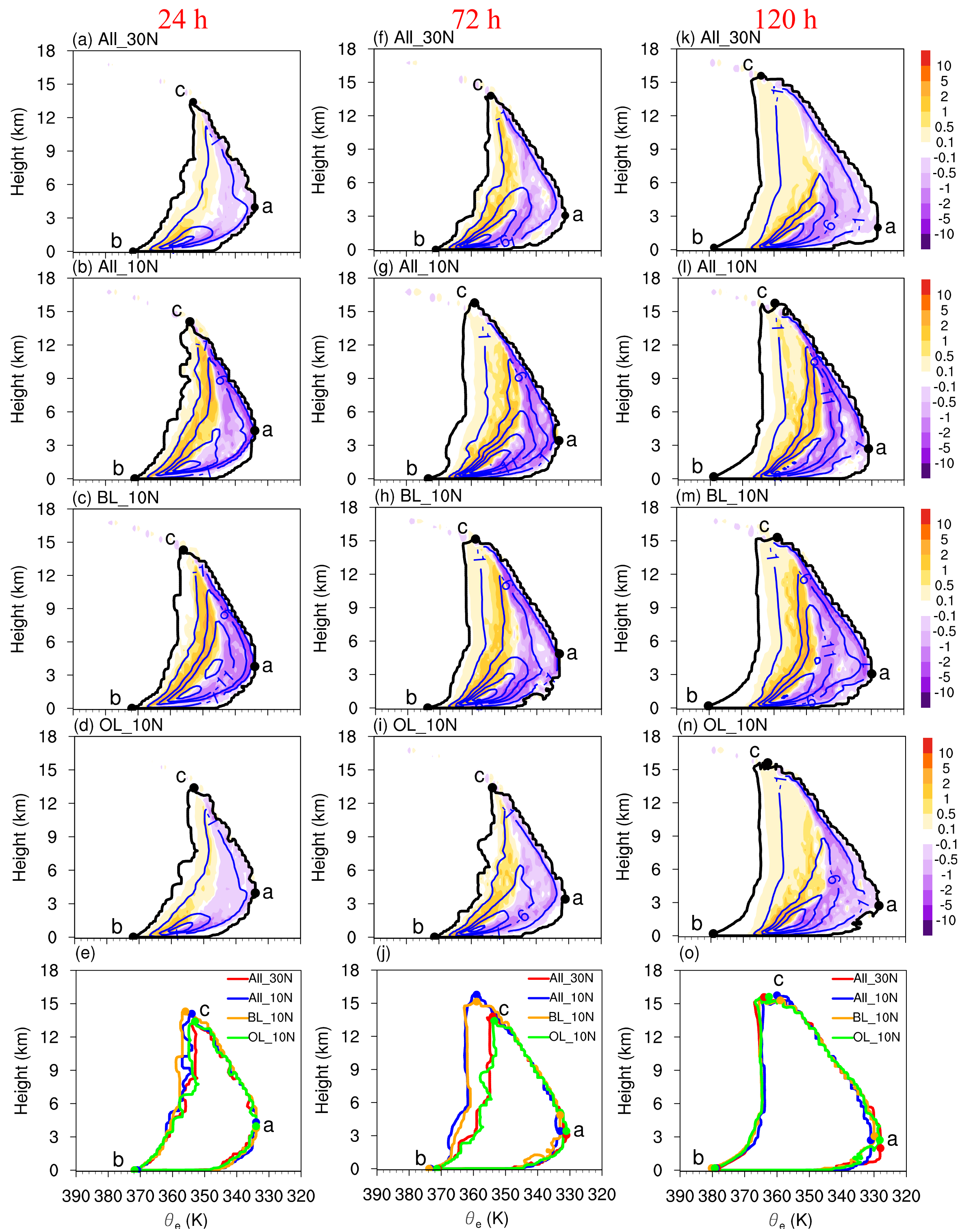

Figure 5. Isentropic vertical mass flux $\langle \rho w' \rangle_{\theta_e}$ (shading; 10^9 kg s^{-1} K^{-1}) and streamfunction (purple contour; 10^9 kg s^{-1}) in $\theta_e - z$ coordinates in the four experiments. The black contours in (a)–(d), (f)–(i), and (k)–(n) and colored contours in (e), (j), and (o) correspond to the streamfunction of 10^7 kg s^{-1}, and the letters "a", "b", and "c" mark the points of the lowest θ_e, the maximum near-surface θ_e, and the highest height.

with

$$w'(r,z,t) = w(r,z,t) - \frac{2\pi\int_0^L \rho(r,z,t)w(r,z,t)rdr}{2\pi\int_0^L \rho(r,z,t)rdr},$$

where ρ and w are the air density and vertical velocity, and w' is the perturbation vertical velocity with the domain-averaged vertical velocity removed to ensure that the contours of Ψ_{θ_e} are closed. The finite-size bins of θ_e and r in this study are in 1 K and 1 km, respectively.

As shown in Pauluis and Mrowiec (2013) and Pauluis (2016), the mean diabatic tendency of air parcel can be expressed by the vertical derivative of Ψ_{θ_e}, and the mean parcel trajectories in isentropic coordinates are along the isolines of Ψ_{θ_e}. Therefore, the isolines of Ψ_{θ_e} can be regarded as the mean "parcel" trajectories with the turbulent flow filtered out. Figure 5 shows Ψ_{θ_e} in the four experiments, in which the flow is clockwise and thus high-θ_e rising air parcels and low-θ_e subsiding air parcels are separated clearly, as discussed in Pauluis and Mrowiec (2013) and Pauluis (2016). Pauluis and Zhang (2017) showed that the heat engine efficiency associated with the deepest overturning circulation or inner-core cycle in isentropic coordinates, defined by the isolines of 2.5% of the minimum of streamfunction, is more comparable with that in the Carnot cycle than that with the shallower overturning circulation. Fang et al. (2019) also confirmed that the deepest overturning circulation is much more pertinent to the intensification of Hurricane Edouard (2014). Therefore, similar to Fang et al. (2019), we focus on the energy cycle associated with the deepest overturning circulation. Considering the minimum of streamfunction varies with time and experiments, to ensure a fair comparison, we define the deepest overturning circulation based on the constant streamfunction isolines of 10^7 kg s^{-1} rather than the relative value to the minimum streamfunction, as depicted by the contours in Fig. 5. For convenience, three letters "a", "b", and "c" are used to denotes the points of the lowest θ_e, the maximum near-surface θ_e, and the highest height, and "ab", "bc", and "ca" denote the inflow leg, ascending leg, and descending leg in the deepest cycle.

We can see that the deepest cycles in All_10N and BL_10N are deeper than those in All_30N and OL_10N during the intensification stages (before 120 h; Figs. 5e,j), especially the ascending leg (bc), consistent with the stronger secondary circulation in Eulerian coordinates and higher outflow layer, which is associated with the weak resistance to convergent inflow in the boundary layer (Fig. 2; Fig. 3). The higher ascending leg indicates that the temperature of the outflow-layer air parcel is lower, consistent with a higher heat engine efficiency (Eq. 4). We thus hypothesize that the more rapid intensification in All_10N and BL_10N than that in All_30N and OL_10N during the earlier intensification stages is largely associated with the deeper heat engine cycle, which will be detailed in the following subsection.

c. Evolution of energy conversion in the simulated TCs

Based on the closed MAFALDA trajectories, i.e., the deepest overturning circulation, we can diagnose the evolution of energy conversion in the four experiments based on Eqs. (4) and (5). As in Pauluis and Mrowiec (2013) and Pauluis (2016), for each thermodynamic variable a, we use its mass-weighted conditional average to filter out fast and reversible oscillatory motions such as gravity waves by Eq. (7) and

$$a(\theta_e, z, t) = \frac{\langle \rho a \rangle_{\theta_e}(\theta_e, z, t)}{\langle \rho \rangle_{\theta_e}(\theta_e, z, t)}. \tag{9}$$

Then all the conditionally averaged thermodynamic variables are interpolated along the MAFALDA trajectories for energy diagnostics.

The $T - s$ diagram based on the conditionally averaged T and s is shown in Figs. 6a–c. As detailed in Fang et al. (2019), the air parcel gains energy by turbulent mixing and surface heating in the inflow leg (ab), and loses energy by detrainment and mixing in the ascending leg (bc) and radiation in the descending leg (ca). The heat engine gains energy at warmer temperature and loses energy at colder temperature, and thus continuously extracting external heat energy and converting it into mechanical energy as a Carnot heat engine (Eq. 4). However, unlike the classical Carnot heat engine as proposed in Emanuel (1986, 1991), the descending leg (ca) is not isothermal nor adiabatic (Figs. 6a–c), with marked thermal stratification in the TC outer core region, as mentioned earlier. This confirms that the hypothesized classical Carnot heat engine (Emanuel 1986, 1991) is not closed in the simulated TCs, and thus the corresponding energy diagnostics in Rappin et al. (2011) could not be justified. The other difference from the classical Carnot heat engine is that the TC heat engine efficiency is limited by the hydrological cycle (W_P and G_P in Eq. 4). As shown in Pauluis and Zhang (2017), the Gibbs penalty is dominated by the cycle of water vapor, as the contents of liquid water and ice and their associated variations of specific Gibbs free energy are much smaller than that of water vapor. Based on the definition of Gibbs free energy of water vapor ($g_v \approx R_v T ln \mathcal{H}$; Eq. A3a), the air parcel gradually gains water vapor from mixing with external clouds in the descending leg (ca) and surface evaporation in the inflow leg (ab) at unsaturated state with lower g_v, but loses water vapor by condensation and precipitation in the ascending leg (bc) at saturated state with lower g_v (Figs. 6d–f), implying a reduction of the mechanical output by the heat engine.

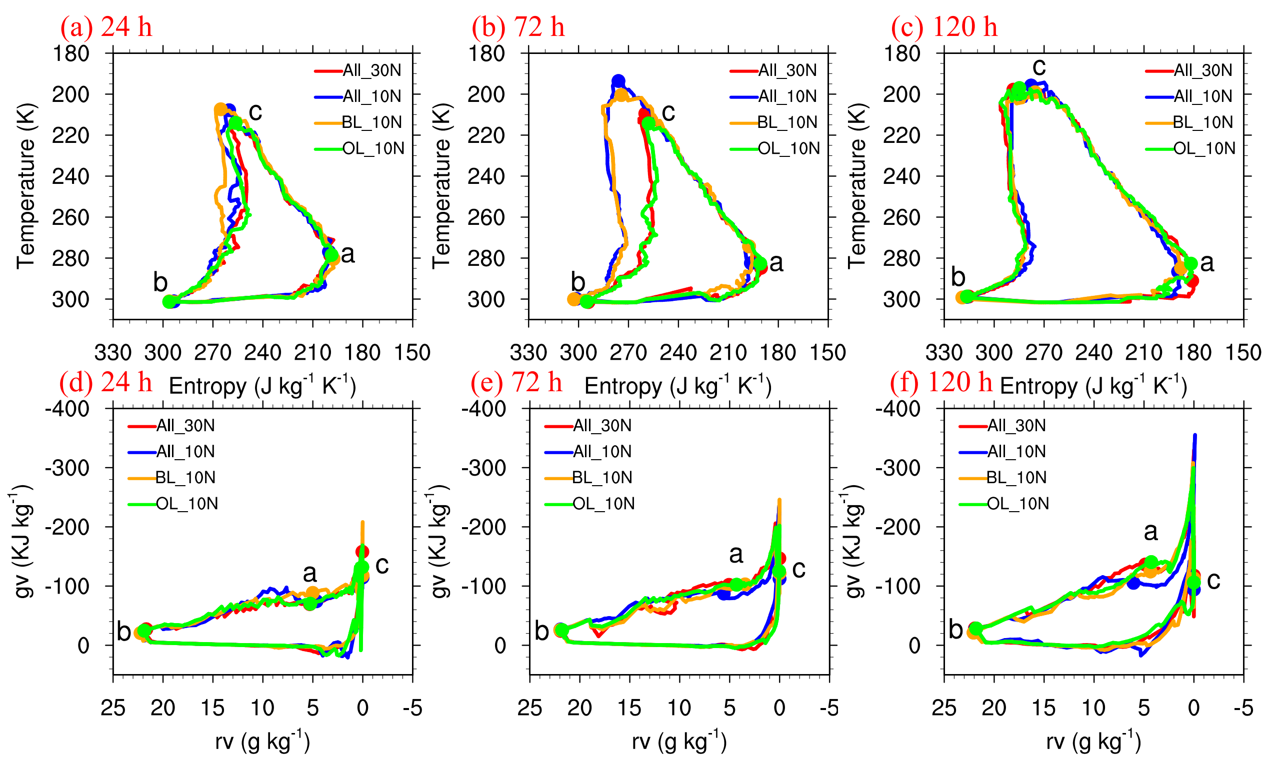

Figure 6. (a)–(c) $T - s$ diagram and $g_v - r_v$ diagram for the MAFALDA trajectories in the four experiments. The letters "a", "b", and "c" mark the corresponding points of the lowest θ_e, the maximum near-surface θ_e, and the highest height in $\theta_e - z$ coordinates. Note that r_v along all trajectories in (d)–(f) is non-negative.

As implied from Figs. 5e,j, the deeper cycle or higher ascending leg in All_10N and BL_10N during the intensification stages corresponds well with a cooler temperature of the energy sink in the heat engine than that in All_30N and OL_10N (Figs. 6a,b), which indicates a higher energy ($\oint Tds$) for producing mechanical work. Figure 7 further shows the time evolutions of those energy terms in Eq. (4) with W_{KE} calculated using Eq. (5), in which results in the initial adjustment stages of the model simulations (~20 h) are excluded. As expected, during the intensification stages the maximum work is higher in All_10N and BL_10N than in All_30N and OL_10N (Fig. 7a), consistent with a higher generation of kinetic energy (Fig. 7b). Similar to that in Pauluis and Zhang (2017) and Fang et al. (2019), both the water lifting W_P (Fig. 7c) and Gibbs penalty G_P (Fig. 7d) reduce the generation of kinetic energy, but compared with W_{max} and W_{KE}, W_P and G_P show smaller magnitude and variation during the TC development. Note that the residual term of Eq. 4 is much smaller than any other terms during all simulation period (Fig. 7e), indicating that MAFALDA can well capture the thermodynamic cycle in the simulated TCs almost during all stages of the TC development, although MAFALDA is based on a statistically steady system. Figure 7f also shows that in isentropic coordinates the vertical divergence of vertical mass flux ($\partial\langle\rho w\rangle_{\theta_e}/\partial z$) is much larger than the local change of the mass ($\partial\langle\rho\rangle_{\theta_e}/\partial t$) even during the intensification period (before 120 h) for all experiments, indicating that the assumption of statistically quasi-steady system may still apply to the intensification stage (Pauluis and Mrowiec 2013).

Rappin et al. (2011) hypothesized that the mechanical dissipation in the isothermal descending leg (leg 3) of the Carnot heat engine in Emanuel (1986, 1991) affects the low-level mechanical dissipation or generation of kinetic energy. Here, the mechanical dissipation along the entire descending leg (ca) in the MAFALDA trajectories has been examined by integrating Eq. (2) as

$$\int_c^a \boldsymbol{F}\cdot d\boldsymbol{l} = -\int_c^a \left[d\left(\frac{1}{2}|\boldsymbol{V}|^2\right) + d(\Gamma z) + \alpha_d dp + \Gamma r_T dz\right]. \qquad (10)$$

As we can see from Fig. 8a, the descending-leg mechanical dissipations in all experiments are similar and close to zero with some small variations during the whole simulation period. This is understandable because the friction and mixings in the outflow and outer-core region are generally much smaller than that in the boundary layer inflow and in the inner-core region (e.g., Heng et al. 2017). This means that the mechanical dissipation following the outflow downstream does not depend on the local inertial stability and the strength of the outflow or the TC intensity, and contributes little to the overall energy conversion and thus TC development, which is in contrast with the hypothesis in Rappin et al. (2011). As expected, the integrated mechanical dissipation (as in Eq. 10) following the inflow and ascending legs (ab+bc) dominates the evolution of the total mechanical dissipation (Fig. 7b; Fig. 8b), consistent with the larger friction and mixings in the boundary-layer inflow and inner-core ascending legs (Li et al. 2019; Heng et al. 2017).

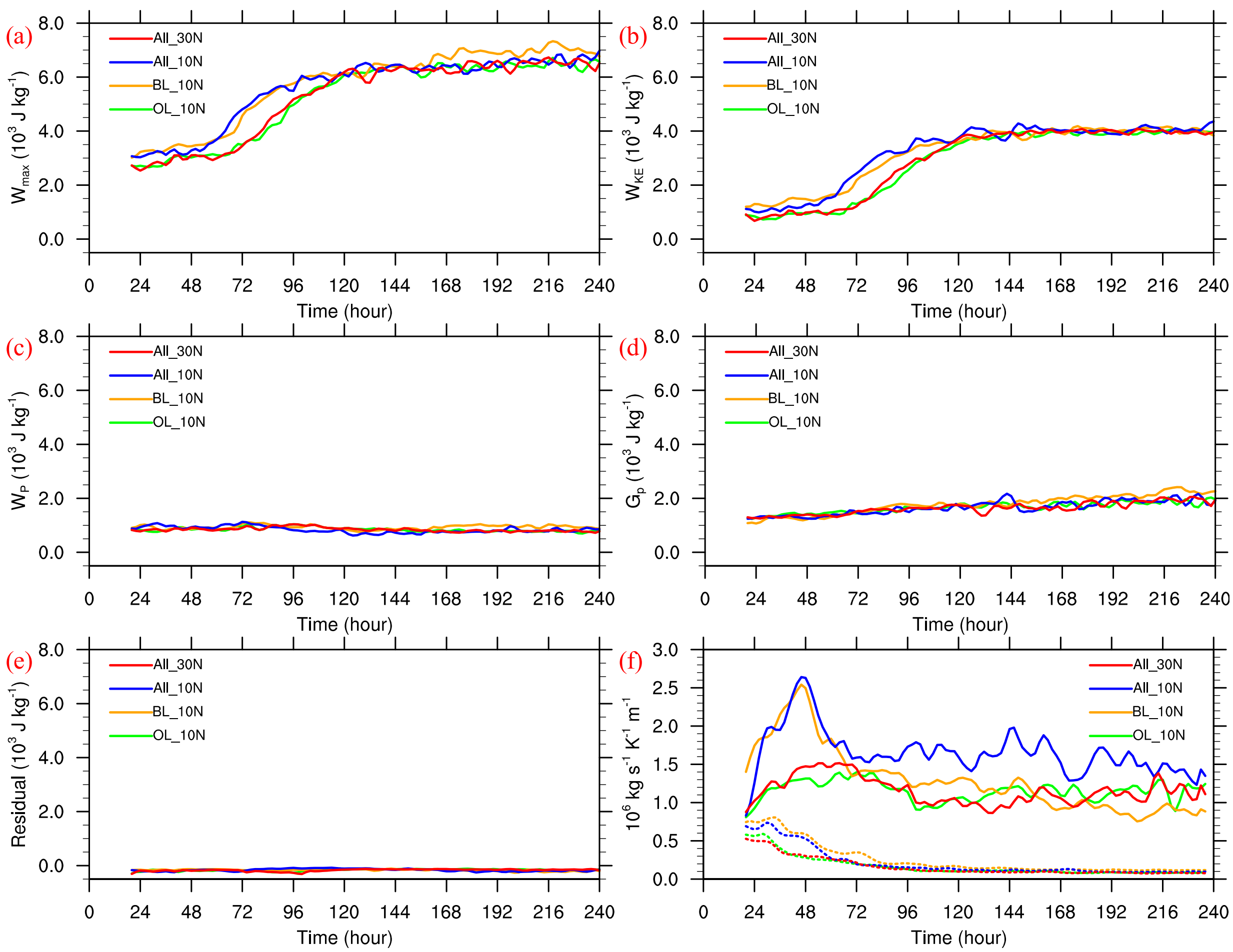

Figure 7. Time series of (a) the maximum work W_{max} ($\oint Tds$), (b) the mechanical dissipation W_{KE} ($-\oint \alpha_d dp - W_P$), (c) work done to lift water W_P ($\oint \Gamma r_T dz$), (d) Gibbs penalty G_P ($-\oint \sum_{w=v,l,i} g_w dr_w$), and (e) the residual term of Eq. 4 ($W_{max} - W_{KE} - W_P - G_P$) based on the deepest MAFALDA cycle in the four experiments. (f) Time series of the absolute values of local change of the mass ($\partial\langle\rho\rangle_{\theta_e}/\partial t$; dashed lines) and vertical divergence of vertical mass fluxes ($\partial\langle\rho w\rangle_{\theta_e}/\partial z$; solid lines) averaged within the deepest MAFALDA cycle in the four experiments.

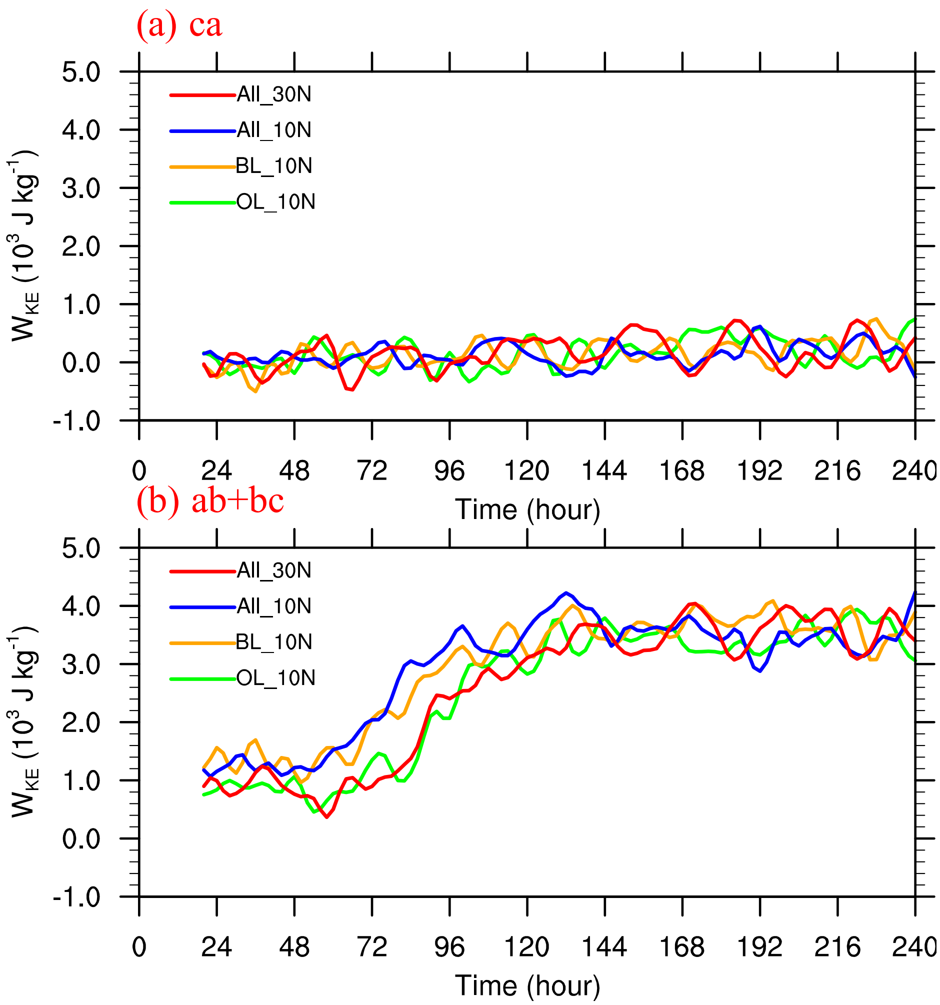

Figure 8. Time series of mechanical dissipation ($\int \boldsymbol{F} \cdot d\boldsymbol{l}$) along (a) the descending leg (ca) and (b) the boundary-layer inflow and ascending legs (ab+bc) based on the deepest MAFALDA cycle in the four experiments.

d. An energetics-based understanding

Similar to that in Fang et al. (2019) but unlike in Rappin et al. (2011), we consider the mechanical dissipation as a whole (i.e., W_{KE}) rather than piecewise as W_{KE} corresponds well with TC intensification (Figs. 1a, 7b; Fang et al. 2019). This is because the TC intensification is generally consistent with the development of the whole TC system. Based on the above results, an energetics-based perspective can help understand the effect of environmental inertial stability on TC development. In All_10N and BL_10N, the weaker resistance to radial motion due to lower global or boundary-layer inertial stability allows a stronger boundary-layer inflow and eyewall updraft than in All_30N and OL_10N (Figs. 2 and 3). The stronger eyewall updraft implies less detrainment and mixing in the ascending leg (Fang and Pauluis 2019) and also a higher and stronger outflow (Figs. 2a–h; Figs. 5e,j) and thus a cooler temperature of the energy sink in the overall TC heat engine cycle (Figs. 6a–c), which results in a higher energy ($\oint Tds$) for producing mechanical work or kinetic energy (Figs. 7a,b). In addition, the higher initial boundary-layer entropy (point b) corresponding to the enhanced surface wind and heat flux in All_10N and BL_10N may also contribute to the stronger eyewall updraft during the primary intensification period than in All_30N and OL_10N (Fig. 6b).

To confirm that the higher theoretical maximum work ($W_{max} = \oint Tds$) in All_10N and BL_10N than in All_30N and OL_10N is dominated by the cooler temperature of the energy sink (T_{out}) in the former, budgets of T_{out} and heat engine efficiency are performed. Along the MAFALDA cycle, the net external heating increment is given by

$$dq = Tds + \sum_{w=v,l,i} g_w dr_w. \tag{11}$$

As in Pauluis and Zhang (2017) and Fang et al. (2019), the total energy source Q_{in} and energy sink Q_{out} along the cycle can be estimated by

$$Q_{in} = \oint \max(dq, 0), \text{ and} \tag{12a}$$

$$Q_{out} = \oint \min(dq, 0). \tag{12b}$$

The temperatures of energy source T_{in} and sink T_{out} over the MAFALDA cycle are calculated using the equations below

$$\frac{Q_{in}}{T_{in}} = \oint \max(\frac{\delta q}{T}, 0), \text{ and} \tag{13a}$$

$$\frac{Q_{out}}{T_{out}} = \oint \min(\frac{\delta q}{T}, 0). \tag{13b}$$

The Carnot efficiency ϵ_C and TC heat engine efficiency ϵ_T over the MAFALDA cycle are defined as

$$\epsilon_C = \frac{T_{in} - T_{out}}{T_{in}}, \text{ and} \tag{14a}$$

$$\epsilon_T = \frac{W_{KE}}{Q_{in}}. \tag{14b}$$

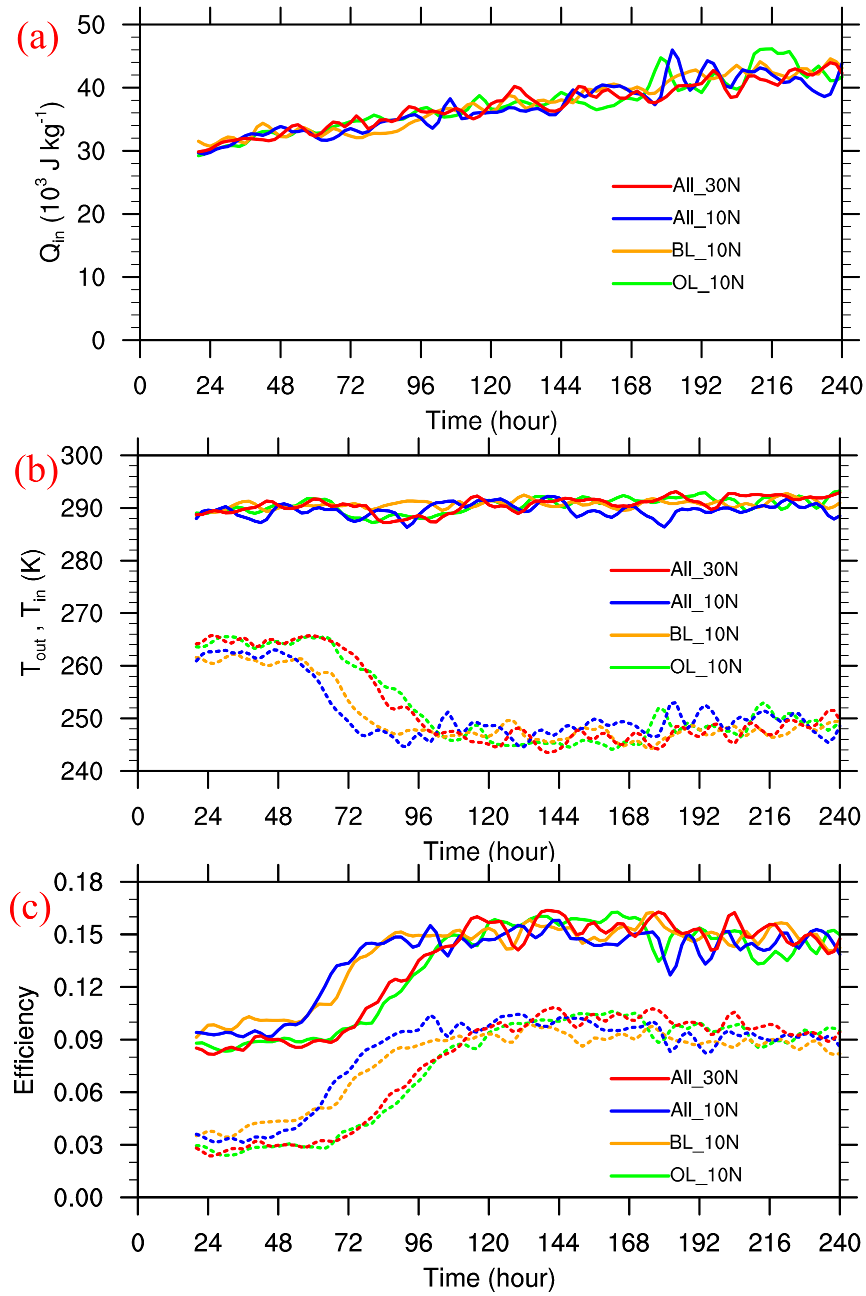

Figure 9. Time series of (a) the energy source Q_{in}, (b) the temperature of energy source T_{in} (solid) and sink T_{out} (dashed), and (c) the Carnot heat engine efficiency (solid) and the TC heat engine efficiency (dashed) in the four experiments.

Since W_{max} is determined by Q_{in} and ϵ_C by definition ($W_{max} \approx \epsilon_C Q_{in}$), we first check the evolution of energy source Q_{in} in the four experiments (Fig. 9a). We can see that there is no significant difference in Q_{in} among the four experiments, consistent with the slight difference in the inflow leg (ab) among the four experiments (Figs. 6a–c), which dominates the energy source in the MAFALDA cycle mainly by surface heating (Fang et al. 2019). This means that the difference in peak boundary-layer entropy between those experiments as mentioned earlier contributes little to the overall Q_{in}. Figure 9b shows the estimated T_{in} (solid) and T_{out} (dashed). As expected, no obvious difference can be found in T_{in} among the four experiments, whereas T_{out} is obviously cooler in All_10N and BL_10N than in All_30N and OL_10N during the intensification stages, consistent with the higher ascending leg (bc) in the former (Figs. 5e,j, 6a,b). The cooler T_{out} results in a higher Carnot efficiency ϵ_C (Eq. 14a; solid in Fig. 9c). As a result, W_{max} ($\approx \epsilon_C Q_{in}$) and thus W_{KE} ($\approx \epsilon_C Q_{in} - W_P - G_P$) are larger in All_10N and BL_10N than in All_30N and OL_10N (Figs. 7a,b), which is consistent with the earlier and more rapid intensification in the earlier intensification stage in the former (Fig. 1a). Figure 9c confirms that ϵ_T (dashed) follows well ϵ_C in all experiments. As shown in Pauluis and Zhang (2017), the TC heat engine in the MAFALDA cycle can produce ~60–70% as much W_{KE} as a Carnot cycle during the steady state (after ~120 h).

Note that although the outflow with a lower outflow-layer inertial stability in OL_10N was enhanced and extended to a larger radius to some extent, the upward motion in the eyewall did not reach the height reached in BL_10N (Figs. 2, 5, 6). Therefore, the boundary-layer inertial stability plays a much more important role in TC development than the outflow-layer inertial stability, as the former dominantly controls the depth of eyewall convection (Figs. 2, 5, 6) and thus the temperature of energy sink (Fig. 9b), TC heat engine efficiency (Fig. 9c), and overall generation of kinetic energy (Figs. 7a,b).

5. Summary and discussion

Previous studies have shown that TCs at a lower latitude tend to develop more rapidly in idealized numerical simulations (e.g., DeMaria and Pickle 1988; Rappin et al. 2011; Li et al. 2011; Smith et al. 2015). This has been explained by the weaker environmental inertial stability, which has weaker resistance to radial motions in both the boundary layer and the outflow layer and thus the secondary circulation. However, it is unclear whether the stronger secondary circulation and more rapid intensification at a lower latitude is dominated by the boundary-layer or outflow-layer dynamics. This has been addressed in this study by a series of ensemble axisymmetric simulations by artificially modifying the Coriolis parameter either in the boundary layer or in the outflow layer. Results show that lowering the outflow-layer Coriolis parameter has little effect on the simulated TC development, whereas lowering the boundary-layer Coriolis parameter leads to much earlier onset of rapid intensification, with the stronger secondary circulation, including the outflow. The results suggest that TC outflow is more likely a passive response to eyewall updraft and convergent inflow in the boundary layer and the local inertial stability in the outflow layer is secondary to TC intensification. This is in contrast to the hypothesis in some previous studies (e.g., Rappin et al. 2011).

The TC development has been widely understood based on the energetics in the literatures (e.g., Tang and Emanuel 2012; Pauluis and Zhang 2017; Fang et al. 2019). Rappin et al. (2011) argued that as the outflow exhausts/ventilates at a larger radius, the energy expenditure on forced subsidence following the outflow downstream may be reduced by additional radiative cooling in the TC Carnot cycle proposed in Emanuel (1986, 1991), and thus more mechanical energy is used against surface frictional dissipation. However, O’Neill and Chavas (2020) argued that the subsidence following the outflow downstream is not “mechanical subsidence”. In addition, the energy of the forced subsidence has not been explicitly characterized in the TC Carnot cycle. Although the radiative cooling-induced subsidence is generally comparable with the actual subsidence in the outer core of a TC (Emanuel 2004; Wang and Lin 2020), this means that the change in entropy is dominated by radiative cooling (Wang and Lin 2020) but is nothing to do with the values of local mechanical work. A detailed examination on the framework of the TC Carnot cycle shows that the isothermal and adiabatic compression legs in the classical Carnot cycle cannot be found in the TC thermodynamic cycle. This suggests that the TC Carnot cycle proposed in Emanuel (1986, 1991) is not closed, implying that the argument on the outflow-layer mechanical work in Rappin et al. (2011) could not be justified.

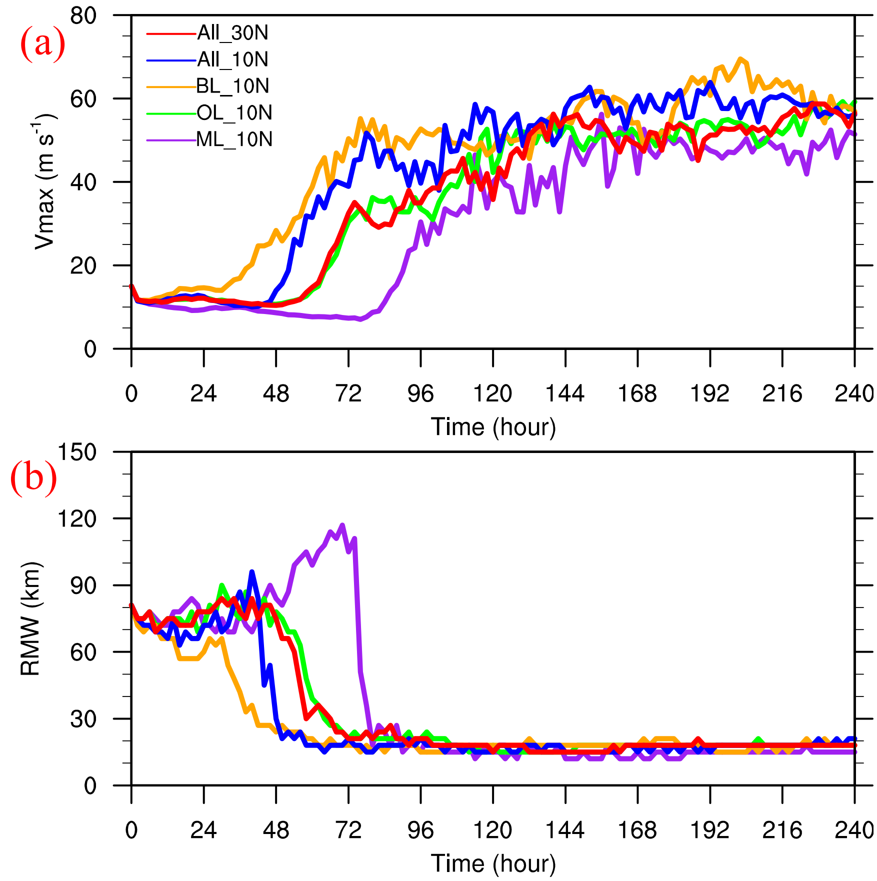

Figure 10. Time series of (a) the azimuthal-mean maximum 10-m tangential wind speed and (b) the corresponding RMW as shown in Fig. 1 but from the three-dimensional version of CM1 with a single run for each experiment.

To understand how the environmental inertial stability affects TC energy cycle and development, we have performed energetics diagnostics based on the isentropic analysis technique MAFALDA (Pauluis and Mrowiec 2013; Pauluis 2016; Mrowiec et al. 2016). Results show that the mechanical dissipation in the descending leg of the MAFALDA cycle is rather small (around zero) with negligible differences among different experiments with varying environmental inertial stability. This means that the low-level or inner-core mechanical dissipation does not depend on the mechanical dissipation following the outflow downstream, which is in contrast with the hypothesis in Rappin et al. (2011). Rather, the overall mechanical work is dominated by the theoretical maximum work in the TC heat engine associated with the energy source and temperatures of energy source and sink. Based on the energetics diagnostics, an energetics-based understanding on the effect of environmental inertial stability on TC development is proposed. Namely, the environmental inertial stability affects TC development mainly through the boundary-layer inertial stability, which controls the convergent inflow and depth of eyewall convection and thus the temperature of energy sink, TC heat engine efficiency, and overall mechanical output or generation of kinetic energy during the intensification stage.

Note that the main results discussed in this study are based on the axisymmetric model simulations. To confirm the robustness of the results, additional five experiments as All_30N, All_10N, BL_10N, OL_10N, and ML_10N but using the three-dimensional version of CM1 and a single simulation for each experiment are conducted with the results shown in Fig. 10. The main difference between in the axisymmetric (Fig. 1a) and three-dimensional (Fig. 10) simulations lies in that the differences of the onset timing of intensification between All_10N and BL_10N and between All_30N and ML_10N are enlarged in the three-dimensional simulations. As mentioned earlier, the difference in the onset timing of intensification between All_10N and BL_10N or between All_30N and ML_10N is due to the difference in the middle-layer inertial stability and thus the feedback between TC circulation and diabatic heating as implied by the balanced vortex dynamics. Unlike in the axisymmetric simulations, convection, and thus diabatic heating, in the three-dimensional simulations is often not organized into concentric rings during the spin-up period, and thus the azimuthally averaged diabatic heating rate is often weaker than that in the axisymmetric simulations (Persing et al. 2013). As a result, the feedback implied by the balanced vortex dynamics during the spin-up period may be more vulnerable to the detrimental effects in the three-dimensional simulations than in the axisymmetric simulations, such as the reduced middle-layer inertial stability in our experiments. This may partly explain the enlarged differences in the three-dimensional simulations compared with those in the axisymmetric simulations. A detailed analysis on the differences in the sensitivity experiments between the axisymmetric and three-dimensional simulations is beyond the scope of the study. Nevertheless, results from the corresponding three-dimensional experiments confirm that the main conclusion based on the axisymmetric simulations, i.e., the earlier and more rapid development of TCs at a lower latitude is due to the weaker inertial stability in the boundary layer rather than that in the outflow layer, is robust. This suggests that more attention should be given to the boundary layer process to understand TC intensity changes.

Finally, we should point out that although the outflow-layer structure is generally quasi-axisymmetric in the idealized three-dimensional simulations with quiescent environment (Rappin et al. 2011), the outflow-layer structure of TCs in reality is often highly asymmetric due to the TC-environment interactions (Black and Anthes 1971; Chen and Gray 1985). Previous studies have shown that the upper-tropospheric troughs or cold-core vortices may facilitate TC intensification by providing asymmetric outflow channels and thus eddy momentum flux for TC development (Merrill 1988; Molinari and Vollaro 1989; Leroux et al. 2016), while some troughs may introduce strong vertical wind shear and thus prevent TC intensification (Hanley et al. 2001; Peirano et al. 2016; Komaromi and Doyle 2018). Although our results suggest that the outflow-layer inertial stability is not crucial to the TC development in a quiescent environment, it may affect the intrusion of environmental forcing in the outflow layer or TC-environment interaction and thus TC development in nature. To further explore the effect of the outflow-layer inertial stability on TC development under different environmental conditions (e.g., outflow-layer troughs) will be a topic of future study.

Acknowledgments.

The authors are grateful to Dr. Daniel Stern and two anonymous reviewers for their constructive review comments. Y. Li thanks Dr. Juan Fang and Dr. Danyang Wang for helpful discussions in the early stage of this study. This study was supported in part by National Natural Science Foundation of China under grants 42192555, 41730960, 61827901, and 42205001. Y. Wang is supported by NSF grant AGS-1834300. Y. Li is also supported partly by China Postdoctoral Science Foundation (BX2021121; 2021M700066).

Data Availability Statement.

The CM1 source code, initial conditions, and model configuration files are available at the website: https://box.nju.edu.cn/d/00347841706d482aa58e/.

APPENDIX

Definition of some thermodynamic variables

Following Pauluis (2016) and Pauluis and Zhang (2017), the thermodynamic reference state is defined as liquid water at the freezing temperature. The entropy per unit mass of dry air is defined as

$$s = s_d + s_v + s_l + s_i, \tag{A1}$$

where the specific entropies of dry air s_d, water vapor s_v, liquid water s_l, and ice s_i are

$$s_d = C_p ln\frac{T}{T_f} - R_d ln\frac{p}{p_0}, \tag{A2a}$$

$$s_v = C_l ln\frac{T}{T_f} + \frac{L_v}{T} - R_v ln\mathcal{H}, \tag{A2b}$$

$$s_l = C_l ln\frac{T}{T_f}, \tag{A2c}$$

$$s_i = C_i ln\frac{T}{T_f} - \frac{L_f}{T_f}, \tag{A2d}$$

where C_p, C_l, and C_i are the specific heat of dry air, liquid water, and ice at constant pressure, T_f and p_0 are the reference temperature (273.15 K) and reference pressure (1000 hPa), R_d and R_v are the gas constant for dry air and water vapor, L_v and L_f are the latent heat of vaporization at T and latent heat of fusion at T_f, and $\mathcal{H}$ is the relative humidity.

The specific Gibbs free energy for water vapor, liquid water, and ice at the reference state T_f are

$$g_v = C_l\left(T - T_f - T ln\frac{T}{T_f}\right) + R_v T ln\mathcal{H}, \tag{A3a}$$

$$g_l = C_l\left(T - T_f - T ln\frac{T}{T_f}\right), \tag{A3b}$$

$$g_i = C_i\left(T - T_f - T ln\frac{T}{T_f}\right) - L_f(1 - \frac{T}{T_f}). \tag{A3c}$$

The equivalent potential temperature θ_e with respect to ice at the reference state with T_f is defined as

$$(C_p + C_i r_T) ln\frac{\theta_e}{T_f} = \left[C_p + r_i C_i + (r_v + r_l) C_l\right] ln\frac{T}{T_f} - R_d ln\frac{p}{p_0} + (r_v + r_l)\frac{L_f}{T_f} + \frac{r_v L_v}{T} - r_v R_v ln\mathcal{H}. \tag{A4}$$

REFERENCES

Black, P. G., and R. A. Anthes, 1971: On the asymmetric structure of the tropical cyclone outflow layer. *J. Atmos. Sci.*, **28**, 1348–1366, https://doi.org/10.1175/1520-0469(1971)028<1348:OTASOT>2.0.CO;2.

Black, P. G., E. A. D'Asaro, W. M. Drennan, J. R. French, P. P. Niiler, T. B. Sanford, ... and J. A. Zhang, 2007: Air–sea exchange in hurricanes: Synthesis of observations from the coupled boundary layer air–sea transfer experiment. *Bull. Amer. Meteor. Soc.*, **88**, 357-374, https://doi.org/10.1175/BAMS-88-3-357.

Bryan, G. H., and J. M. Fritsch, 2002: A benchmark simulation for moist nonhydrostatic numerical model. *Mon. Wea. Rev.*, **130**, 2917–2928, https://doi.org/10.1175/1520-0493(2002)130,2917: ABSFMN.2.0.CO;2.

Challa, M., and R. L. Pfeffer, 1980: Effects of eddy fluxes of angular momentum on model hurricane development. *J. Atmos. Sci.*, **37**, 1603–1618, https://doi.org/10.1175/1520-0469(1980)037,1603: EOEFOA.2.0.CO;2.

Chen, L. S., and W. M. Gray, 1985: Global view of the upper level outflow pattern associated with tropical cyclone intensity changes during FGGE. Dept. of Atmos. Sci. Paper No. 392, Colorado State University, Ft. Collins, CO, USA, 126.

Chen, X.-M., Y. Wang, and K. Zhao, 2015: Synoptic flow patterns and large-scale characteristics associated with rapidly intensifying tropical cyclones in South China Sea, *Mon. Wea. Rev.*, **143**, 64–87, https://doi.org/10.1175/MWR-D-13-00338.1.

Dai, Y., S. J. Majumdar, and D. S. Nolan, 2021: Tropical cyclone resistance to strong environmental shear. *J. Atmos. Sci*., **78**, 1275–1293, https:// doi.org/10.1175/JAS-D-20-0231.1.

DeMaria, M., and J. D. Pickle, 1988: A simplified system of equations for simulation of tropical cyclones. *J. Atmos. Sci.*, **45**, 1542–1554, https://doi.org/10.1175/1520-0469(1988)045,1542:ASSOEF.2.0.CO;2.

Ditchek, S. D., J. Molinari, and D. Vollaro, 2017: Tropical cyclone outflow-layer structure and balanced response to eddy forcings. *J. Atmos. Sci.*, **74**, 133–149, https://doi.org/10.1175/JAS-D-16-0117.1.

Donelan, M. A., B. K. Haus, N. Reul, W. J. Plant, M. Stiassnie, H. C. Graber, O. B. Brown, and E. S. Saltzman, 2004: On the limiting aerodynamic roughness of the ocean in very strong winds. *Geophys. Res. Lett.*, **31**, L18306, https://doi.org/10.1029/ 2004GL019460.

Emanuel, K. A., 1986: An air-sea interaction theory for tropical cyclones. Part I: Steady state maintenance. *J. Atmos. Sci.*, **43**, 585–605, https://doi.org/10.1175/1520-0469(1986)043,0585: AASITF.2.0.CO;2.

Emanuel, K. A., 1991: The theory of hurricanes. *Annu. Rev. Fluid Mech.*, **23**, 179–196, https://doi.org/10.1146/annurev.fl.23.010191.001143.

Emanuel, K. A., 1997: Some aspects of hurricane inner-core dynamics and energetics. *J. Atmos. Sci.*, **54**, 1014–1026, https://doi.org/10.1175/1520-0469(1997)054,1014:SAOHIC.2.0.CO;2.

Emanuel, K. A., 2004: Tropical cyclone energetics and structure. *Atmospheric Turbulence and Mesoscale Meteorology*, E. Federovich, R. Rotunno, and B. Stevens, Eds., Cambridge University Press, 165–192, https://doi.org/10.1017/CBO9780511735035.010.

Emanuel, K. A., 2012: Self-stratification of tropical cyclone outflow. Part II: Implications for storm intensification. *J. Atmos. Sci*., **69**, 988–996, https://doi.org/10.1175/JAS-D-11-0177.1.

Emanuel, K. A., and R. Rotunno, 2011: Self-stratification of tropical cyclone outflow. Part I: Implications for storm structure. *J. Atmos. Sci*., **68**, 2236–2249, https://doi.org/10.1175/JAS-D-10-05024.1.

Emanuel, K. A., 2018: 100 years of progress in tropical cyclone research. *A Century of Progress in Atmospheric and Related Sciences: Celebrating the American Meteorological Society Centennial, Meteor. Monogr.*, No. **59**, Amer. Meteor. Soc., https://doi.org/10.1175/AMSMONOGRAPHS-D-18-0016.1.

Fang, J., O. Pauluis, and F. Zhang, 2019: The thermodynamic cycles and associated energetics of

Hurricane Edouard (2014) during its intensification. *J. Atmos. Sci.*, **76**, 1769–1784, https://doi.org/10.1175/JAS-D-18-0221.1.

Fei, R., Y. Wang, and Y. Li, 2021: Contributions of vertical advection to supergradient wind in tropical cyclone boundary layer: A numerical study. *J. Atmos. Sci.*, **78**, 1057–1073, https://doi.org/10.1175/JAS-D-20-0075.1.

Hanley, D., J. Molinari, and D. Keyser, 2001: A composite study of the interactions between tropical cyclones and upper-tropospheric troughs. *Mon. Wea. Rev.*, **129**, 2570–2584, https://doi.org/10.1175/1520-0493(2001)129,2570:ACSOTI.2.0.CO;2.

Heng, J., Y. Wang, and W. Zhou, 2017: Revisiting the balanced and unbalanced aspects of tropical intensification. *J. Atmos. Sci.*, **74**, 2575–2591, https://doi.org/10.1175/JAS-D-17-0046.1.

Holland, G. J., and R. T. Merrill, 1984: On the dynamics of tropical cyclone structure changes. *Quart. J. Roy. Meteor. Soc.*, **110**, 723–745, https://doi.org/10.1002/qj.49711046510.

Kepert, J., and Y. Wang, 2001: The dynamics of boundary layer jets within the tropical cyclone core. Part II: Nonlinear enhancement. *J. Atmos. Sci.*, **58**, 2485–2501, https://doi.org/10.1175/1520-0469(2001)058,2485:TDOBLJ.2.0.CO;2.

Komaromi, W. A., and J. D. Doyle, 2017: Tropical cyclone outflow and warm core structure as revealed by HS3 dropsonde data. *Mon. Wea. Rev.*, **145**, 1339–1359, https://doi.org/10.1175/MWR-D-16-0172.1.

Komaromi, W. A., and J. D. Doyle, 2018: On the dynamics of tropical cyclone and trough interactions. *J. Atmos. Sci.*, **75**, 2687–2709, https://doi.org/10.1175/JAS-D-17-0272.1.

Leroux, M., M. Plu, and F. Roux, 2016: On the sensitivity of tropical cyclone intensification under upper-level trough forcing. *Mon. Wea. Rev.*, **144**, 1179–1202, https://doi.org/10.1175/MWR-D-15-0224.1.

Li, T., X. Ge, M. Peng, and W. Wang, 2012: Dependence of tropical cyclone intensification on the Coriolis parameter. *Trop. Cyclone Res. Rev.*, **1**, 242–253, https://doi.org/10.6057/2012TCRR02.04.

Li, T.-H., and Y. Wang, 2021a: The role of boundary layer dynamics in tropical cyclone intensification. Part I: Sensitivity to surface drag coefficient. *J. Meteor. Soc. Japan*, **99**, 537–554, https://doi.org/10.2151/jmsj.2021-027.

Li, T.-H., and Y. Wang, 2021b: The role of boundary layer dynamics in tropical cyclone intensification. Part II: Sensitivity to initial vortex structure. *J. Meteor. Soc. Japan*, **99**, 555–573, https://doi.org/10.2151/jmsj.2021-028.

Li, Y., Y. Wang, Y. Lin, and R. Fei, 2020: Dependence of superintensity of tropical cyclones on SST in axisymmetric numerical simulations. *Mon. Wea. Rev.*, **148**, 4767–4781, https://doi.org/10.1175/MWR-D-20-0141.1.

Li, Y., Y. Wang, Y. Lin, and X. Wang, 2021: Why does rapid contraction of the radius of maximum wind precede rapid intensification in tropical cyclones? *J. Atmos. Sci.*, **78**, 3441–3453, https://doi. org/10.1175/JAS-D-21-0129.1.

Li, Y., Y. Wang, and Z.-M. Tan, 2022: How frequently does rapid intensification occur after rapid contraction of the radius of maximum wind in tropical cyclones over the North Atlantic and eastern North Pacific? *Mon. Wea. Rev.*, **150**, 1747–1760, https://doi.org/10.1175/MWR-D-21-0322.1.

McBride, J. L., 1981: Observational analysis of tropical cyclone formation. Part III: Budget analysis. *J. Atmos. Sci.*, **38**, 1152–1166, https://doi.org/10.1175/1520-0469(1981)038%3C1152:OAOTCF%3E2.0.CO;2.

Merrill, R. T., 1988: Characteristics of the upper-tropospheric environmental flow around hurricanes. *J. Atmos. Sci.*, **45**, 1665–1677, https://doi.org/10.1175/1520-0469(1988)045,1665:COTUTE.2.0.CO;2.

Molinari, J., and D. Vollaro, 1989: External influences on hurricane intensity. Part I: Outflow layer eddy angular momentum fluxes. *J. Atmos. Sci.*, **46**, 1093–1105, https://doi.org/10.1175/1520-0469(1989)046,1093:EIOHIP.2.0.CO;2.

Mrowiec, A. A., O. M. Pauluis, and F. Zhang, 2016: Isentropic analysis of a simulated hurricane.

J. Atmos. Sci., **73**, 1857– 1870, https://doi.org/10.1175/JAS-D-15-0063.1.

O’Neill, M. E., and D. R. Chavas, 2020: Inertial waves in axisymmetric tropical cyclones, *J. Atmos. Sci.*, **77**, 2501-2517, https://doi.org/10.1175/JAS-D-19-0330.1.

Oyama, R., 2017: Relationship between tropical cyclone intensification and cloud-top outflow revealed by upper-tropospheric atmospheric motion vectors. *J. Appl. Meteor. Climatol.*, **56**, 2801–2819, https://doi.org/10.1175/JAMC-D-17-0058.1.

Pauluis, O., 2011: Water vapor and mechanical work: A comparison of Carnot and steam cycles. *J. Atmos. Sci.*, **68**, 91–102, https://doi.org/10.1175/2010JAS3530.1.

Pauluis, O., 2016: The mean air flow as Lagrangian dynamics approximation and its application to moist convection. *J. Atmos. Sci.*, **73**, 4407–4425, https://doi.org/10.1175/JAS-D-15-0284.1.

Pauluis, O., and I. M. Held, 2002a: Entropy budget of an atmosphere in radiative–convective equilibrium. Part I: Maximum work and frictional dissipation. *J. Atmos. Sci.*, **59**, 125–139, https://doi.org/10.1175/1520-0469(2002)059,0125:EBOAAI.2.0.CO;2.

Pauluis, O., and I. M. Held, 2002b: Entropy budget of an atmosphere in radiative–convective equilibrium. Part II: Latent heat transport and moist processes. *J. Atmos. Sci.*, **59**, 140–149, https://doi.org/10.1175/1520-0469(2002)059,0140:EBOAAI.2.0.CO;2.

Pauluis, O., and A. A. Mrowiec, 2013: Isentropic analysis of convective motions. *J. Atmos. Sci.*, **70**, 3673–3688, https://doi.org/10.1175/ JAS-D-12-0205.1.

Pauluis, O., V. Balaji, and I. M. Held, 2000: Frictional dissipation in a precipitating atmosphere. *J. Atmos. Sci.*, **57**, 989–994, https://doi.org/10.1175/1520-0469(2000)057,0989:FDIAPA.2.0.CO;2.

Pauluis, O., and F. Zhang, 2017: Reconstruction of the thermodynamic cycles in a high-resolution simulation of a hurricane. *J. Atmos. Sci.*, **74**, 3367–3381, https://doi.org/10.1175/JAS-D-16-0353.1.

Peirano, C. M., K. L. Corbosiero, and B. H. Tang, 2016: Revisiting trough interactions and tropical cyclone intensity change. *Geophys. Res. Lett.*, **43**, 5509–5515, https://doi.org/10.1002/2016GL069040.

Peng, K., R. Rotunno, and G. H. Bryan, 2018: Evaluation of a time-dependent model for the intensification of tropical cyclones. *J. Atmos. Sci.*, **75**, 2125–2138, https://doi.org/10.1175/JAS-D-17-0382.1.

Persing, J., M. T. Montgomery, J. C. McWilliams, and R. K. Smith, 2013: Asymmetric and axisymmetric dynamics of tropical cyclones. *Atmos. Chem. Phys.*, **13**, 13323–13438, https://doi.org/10.5194/acp-13-12299-2013.

Rappin, E. D., M. C. Morgan, and G. J. Tripoli, 2011: The impact of outflow environment on tropical cyclone intensification and structure. *J. Atmos. Sci.*, **68**, 177–194, https://doi.org/10.1175/ 2009JAS2970.1.

Rotunno, R., and K. A. Emanuel, 1987: An air–sea interaction theory for tropical cyclones. Part II: Evolutionary study using a nonhydrostatic axisymmetric numerical model. *J. Atmos. Sci.*, **44**, 542–561, https://doi.org/10.1175/1520-0469(1987)044,0542: AAITFT.2.0.CO;2.

Rousseau-Rizzi, R., and K. Emanuel, 2019: An evaluation of hurricane superintensity in axisymmetric numerical models. *J. Atmos. Sci.*, **76**, 1697–1708, https://doi.org/10.1175/JAS-D-18-0238.1.

Ryglicki, D. R., J. D. Doyle, D. Hodyss, J. H. Cossuth, Y. Jin, K. C. Viner, and J. M. Schmidt, 2019: The unexpected rapid intensification of tropical cyclones in moderate vertical wind shear. Part III: Outflow–environment interaction. *Mon. Wea. Rev.*, **147**, 2919–2940, https://doi.org/10.1175/MWR-D-18-0370.1.

Shi, D., and G. Chen, 2021: The Implication of Outflow Structure for the Rapid Intensification of Tropical Cyclones under Vertical Wind Shear. *Mon. Wea. Rev.* **149**, 4107–4127, https://doi.org/10.1175/MWR-D-21-0141.1.

Shi, J.-J., S. W.-J. Chang, and S. Raman, 1990: A numerical study of the outflow layer of tropical cyclones. *Mon. Wea. Rev.*, **118**, 2042–2055, https://doi.org/10.1175/1520-0493(1990)118<2042:ANSOTO>2.0.CO;2.

Schubert, W. H., and J. J. Hack, 1982: Inertial stability and tropical cyclone development. *J. Atmos. Sci.*, **39**, 1687–1697, https://doi.org/10.1175/1520-0469(1982)039,1687:ISATCD.2.0.CO;2.

Smith, R. K., G. Kilroy, and M. T. Montgomery, 2015: Why do model tropical cyclones intensify more rapidly at low latitudes? *J. Atmos. Sci.*, **72**, 1783–1804, https://doi.org/10.1175/JAS-D-14-0044.1.

Tang, B., and K. Emanuel, 2012: A ventilation index for tropical cyclones. *Bull. Amer. Meteor. Soc.*, **93**, 1901–1912, doi:10.1175/BAMS-D-11-00165.1.

Thompson, G., P. R. Field, R. M. Rasmussen, and W. D. Hall, 2008: Explicit forecasts of winter precipitation using an improved bulk microphysics scheme. Part II: Implementation of a new snow parameterization. *Mon. Wea. Rev.*, **136**, 5095–5115, https://doi.org/10.1175/2008MWR2387.1.

Vigh, J. L., and W. H. Schubert, 2009: Rapid development of the tropical cyclone warm core. *J. Atmos. Sci.*, **66**, 3335–3350, https://doi.org/10.1175/2009JAS3092.1.

Wang, D., and Y. Lin, 2020: Size and structure of dry and moist reversible tropical cyclones. *J. Atmos. Sci.*, **77**, 2091–2114, https://doi.org/10.1175/JAS-D-19-0229.1.

Wang, Y., 2007: A multiply nested, movable mesh, fully compressible, nonhydrostatic tropical cyclone model - TCM4: Model description and development of asymmetries without explicit asymmetric forcing. *Meteor. Atmos. Phys*., **97**, 93–116, https:// doi.org/10.1007/s00703-006-0246-z.

Wang, Y., Y. Li, and J. Xu, 2021: A new time-dependent theory of tropical cyclone intensification. *J. Atmos. Sci.*, **78**, 3855–3865, https:/doi.org/10.1175/JAS-D-21-0169.1.

Wu, C.-C., and H.-J. Cheng, 1999: An observational study of environmental influences on the intensity changes of Typhoons Flo (1990) and Gene (1990). *Mon. Wea. Rev.*, **127**, 3003–3031, https://doi.org/10.1175/1520-0493(1999)127<3003:AOSOEI>2.0.CO;2.

Wood, V. T., and L. W. White, 2011: A new parametric model of vortex tangential-wind profiles: Development, testing, and verification. *J. Atmos. Sci*., **68**, 990–1006, https://doi.org/

10.1175/2011JAS3588.1.

Xu, Y.-M., and Y. Wang, 2013: On the initial development of asymmetric vertical motion and horizontal relative flow in a mature tropical cyclone embedded in environmental vertical shear. *J. Atmos. Sci.*, **70**, 3471–3491. https://doi.org/10.1175/JAS-D-12-0335.1.

Zhang, J. A., and W. M. Drennan, 2012: An observational study of vertical eddy diffusivity in the hurricane boundary layer. *J. Atmos. Sci*., **69**, 3223–3236, https://doi.org/10.1175/JAS-D-11-0348.1.

Zhang, J. A., and M. T. Montgomery, 2012: Observational estimates of the horizontal eddy diffusivity and mixing length in the low-level region of intense hurricanes. *J. Atmos. Sci.*, **69**, 1306–1316, https://doi.org/10.1175/JAS-D-11-0180.1.